Flow Measurement and Instrumentation 79 (2021) 101947

Contents lists available at ScienceDirect

Flow Measurement and Instrumentation

journal homepage: www.elsevier.com/locate/flowmeasinst

# A finite element model for the analysis of flexible tube Coriolis mass flow meter using first order shear deformation shell theory

R. Kamal Krishna [a,b,c], M. Unnikrishnan [a,c,d], Jayaraj Kochupillai [a,c,e,*]

[a] Advanced Dynamics and Control Lab, College of Engineering Trivandrum, India
[b] Assistant Professor of Mechanical Engineering, SCT College of Engineering, Trivandrum, Kerala
[c] Affiliated to APJ Abdul Kalam Kerala Technological University, India
[d] Associate Professor of Mechanical Engineering, College of Engineering, Trivandrum, India
[e] Principal, Mar Baselious College of Engineering & Technology, Pallikkunnu P O, Peermade, Idukki, 685531, Kerala, India

ARTICLE INFO

*Keywords:*
CFM
Flexible tube
Pre-stretch
Beat
Natural frequency
Sensitivity

ABSTRACT

The numerical modelling of Coriolis Mass flow Meter (CFM) is essential for predicting its outcomes accurately in terms of sensitivity as well as exact mass flow rates. In the majority of mathematical and numerical modelling concerning the flexible structures, the authors neglect the dimensional and shape variation of the structure due to self-weight. The shell based on the First-order shear deformation shell theory (FSDST) is preferred in modelling shells compared to the beam model. The current work includes numerical modelling of CFM using eight noded isoparametric shell elements and twenty noded Acoustic fluid elements. The fluid energy describes as the potential, and the dynamic boundary condition is assumed utilising the displacement of structure and potential of the fluid. The fluid dynamic equation combining suitable numerical model, fluid-structure interaction module and cross-correlation technique helps to achieve the numerical modelling of CFM. The numerical model of CFM utilises the Newmark Beta method of numerical integration, and the response of two equidistant locations from the point of tube excitation is acquired. For the flexible tube conveying fluid, there exists sagging of tube due to the weight of tube and fluid. The Coriolis force and the external excitation force cause the fluid conveying tube to bend and twist, and as a result, the velocity responses picked from two equidistant points shows a difference in phase. The effect of sagging leads to a lower phase shift and time decay, and hence the sensitivity of the CFM is low for low pre-stretched flexible tubes. The pre-stretching of flexible tubes reduces the effect of sagging, facilitates to regain the cylindrical shape of the tube and increases the sensitivity of CFM. The result reveals that the shell element along with the three-dimensional acoustic fluid element provides the most accurate numerical model for the CFM and the change in sensitivity, as well as the change in mass flow measurements, can appropriately be analysed with the help of this numerical model. The amplitude of the velocity of the structure, measured from the two equidistant points, shows a difference. The severe variation in amplitude of velocity measured from two points is an implication of the out of plane deflection of the tube. For a CFM made up of metal tubes, the amplitude of velocity variation is minimal and ignored by the authors.

## 1. Introduction

The Coriolis mass flow meter (CFM) consists of an externally vibrating fluid conveying tube, two motion detectors located equidistant from the excitation point and a data acquisition system. The CFM is a globally accepted, precise device that measures the actual mass flow rate and density of the fluid. Within a short duration, CFM gains tremendous applications in industries as an accurate mass flow measurement device as well as calibration flow meter in oil and gas, textile and synthetic, food industries, medical and pharmaceutical sectors. CFM offers include high accuracy in flow measurements, a broad range of operation, and excellent repeatability. As the fluid conveying tube is excited at its fundamental frequency, the fluid experiences directional change for the motion, which results in Coriolis forces. The Coriolis force tends to deform the fluid conveying tube, which results in the same magnitude of force at the inlet and exit regions of the tube. But the direction of Coriolis force at the inlet and exit regions opposes each other, which imparts a phase shift between the responses.

The phase shift can be measured using two motion detectors placed

* Corresponding author.
*E-mail address:* jayaraj@cet.ac.in (J. Kochupillai).

https://doi.org/10.1016/j.flowmeasinst.2021.101947
Received 15 May 2020; Received in revised form 10 February 2021; Accepted 15 April 2021
Available online 19 April 2021

**Nomenclature**

| | |
|---|---|
| $\beta_\xi$, $\beta_\eta$ | Rotation vectors along ξ and η directions |
| $\varepsilon_\xi$, $\varepsilon_\eta$, $\varepsilon_z$ | Normal Strain along ξ, η and z directions |
| $\gamma_{\xi\eta}$, $\gamma_{\eta z}$, $\gamma_{z\xi}$ | Shear strains |
| $\gamma_{0\xi\eta}$, $\gamma_{0\eta z}$, $\gamma_{0z\xi}$ | Shell Mid plane Shear strains |
| $K_\xi$,$K_\eta$ | Radius of curvatures along ξ and η directions |
| $\sigma_\xi$,$\sigma_\eta$ | Normal Stresses in local coordinate system |
| $\tau_{\xi\eta}\tau_{\eta z}, \tau_{z\xi}$ | Shear Stresses in local coordinate system |
| A,B | Lame's Parameters |
| E | Young's Modulus |
| $D_s$ | Constitutive matrix for shell |
| G | Shear Modulus |
| υ | Poisson's ratio |
| $u_0$, $v_0$,$w_0$ | Mid surface displacements of the shell |
| $d_{ei}$ | Generalized Global displacement vector |
| $N_i$ | Shape function for the ith node |
| ξ, η, ζ | Local Coordinates for the shell |
| $\sigma_{ij}$ | Shell element stress |
| $\varepsilon_{ij}$ | Shell element strain |
| $B_s$ | Strain Displacement Matrix of the shell |
| $K_s$ | Shell Stiffness Matrix |
| $K_g$ | Geometric Stiffness Matrix |
| $K_e$ | Kinetic Energy of the shell |
| m | Mass of the shell |
| U | Displacement vector of the shell |
| H | Transformation Matrix |
| Φ | Velocity Potential |
| c | Velocity of Sound |
| $U_z$ | Mean axial flow velocity |
| $V_z$ | Velocity of the shell along the radial direction |
| $V_r$ | Radial Velocity of fluid |
| $P_s$ | Stagnation Pressure |
| $P_p$ | Perturbation Pressure |
| $N_{fi}$ | Shape function of the fluid $i^{th}$node |
| $\Omega_1$, $\Omega_2$ | Frequencies corresponding to the flanks of the peak response |
| $\Omega_n$ | Peak response frequency |
| $\eta_d$ | Damping ratio |
| $\rho_s$ | Density of Silicone tube |
| $\rho_f$ | Density of conveying fluid |
| n | Time step |
| β,γ | Numerical integration parameters |
| P | Effective force |
| $\widehat{K}$ | Effective stiffness |
| Δt | Time step |

at two sections. The mass flow rate of fluid conveying through the tube is proportional to the phase shift or time decay. The ratio of the phase shift to the actual fluid flow rate furnishes the sensitivity of the CFM. The sensitivity of the flow meter is a critical performance parameter for the selection of flow measuring devices. The CFM offers desirable sensitivity with high accuracies. The sensitivity of CFM is usually dependent on the extent of deflection and the twist of the tube. Usually, the metal tube needs more energy to deflect, hence to reduce the energy requirement they are excited at the tube's natural frequencies. Increasing the Coriolis forces in the tube enhances the sensitivity of CFM. Sensitivity improves for the CFM if the tubes of different geometry like u-shape, Ω-shape, and Δ-shape replace the straight tube.

The numerical modelling of CFM helps to identify the operating conditions and sensitivity. The CFMs need accurate numerical modelling as the tube oscillations, and the resultant deformations, as well as the twists in the tube, are tiny in magnitude. The conventional modelling of CFMs was beam model with the fluid as an added mass to the structure. The literature confines the shell modelling of CFMs as the interaction of fluid, and the conveying tube finds difficulty in mathematical, analytical and numerical modelling. The shell model takes care of rotary inertia as well as the shear deformations; hence the twist happened due to the Coriolis forces can be represented accurately using Shell models. The availability of proper mathematical and numerical models for the fluid-structure interaction problems and flow measuring devices are limited. The vibrational behaviour of cylindrical shells conveying fluids subjected to steady loads, pulsatile loads, shock or other transient loadings is significant in the design point of view.

A thorough literature review on CFM reveals that the conventional technique to model CFM tube is using Beam or Shell elements. Beam model is a simple model usually adopted in solving fluid-structure interaction problems, where the fluid models as an added mass to the structure. Beam theory gives reasonable accuracy in predicting fundamental frequencies and responses of CFM, which uses flexible tubes [1]. By the implementation of shear deformations and rotary inertia effects, the Timoshenko beams provide more accurate results in comparison with the Euler-Bernoulli beam model for the fundamental frequencies and responses of CFM.

Beam model for tubes conveying fluids (with the fluid as an added mass to the structure) is not solely desirable for the flexible structures as the pressure acting on the inner tube surface alters the dimensions of the tube in all directions due to Poisson coupling. An attempt to the numerical and analytical modelling of CFMs is prevalent in recent days since the fabrication; characterization and prototype development of these devices are very expensive and time-consuming. The analytical modelling of CFM's is usually limited to straight cylindrical geometries which usually ignore most of the actual physical effects such as sagging of tube and non-homogeneity in tube material. The finite element analysis is a powerful tool which can handle complex geometries.

Several researchers have proposed the numerical formulation of fluid flow problems, which includes fluid-structure interaction (FSI) and flow-induced vibrations. But the finite element analyses of shells conveying fluids are restricted. Paidoussis has performed a detailed investigation of FSI in pipes in his two volumes of the book [2,3]. Ming Ji et al. [4] proposed a mathematical model to examine the vibrational characteristics of the fluid-filled thick cylindrical shells. The FSDST is used to develop the governing equations, and the numerical model extends better accuracy than other numerical models for clamped-clamped pipes with fluid. This work does not involve any flow through pipes. Kochupillai et al. [5] developed a semi analytical-numerical model for elastic shells conveying fluids. The displacement-based axisymmetric eight noded shell elements have opted for structural modelling for viscoelastic pipes. They use a velocity-potential based fluid model; use Bernoulli's equation for deriving the fluid pressure acting on the pipe walls. Amabili et al. [6], Tubaldi et al. [7], Zhang et al. [8] modelled thin circular cylindrical shells conveying fluids. They found that the Surface stresses, flexibility in boundary conditions, the thickness of the thin-walled shell, initial tension, hydrostatic pressure and flow velocity has a strong influence in the vibrational characteristics of the shell. Sadowski et al. [9] and Keramat et al. [10] modelled thick fluid conveying pipes using the shell model. They pointed out that the thick shell treatment gives accurate results for buckling moment under uniform bending for very thick and long cylinders.

Ruoff et al. [11] presented an accurate numerical model using Timoshenko beam theory and a model reduction technique for CFM made up of a pipe with arbitrary geometry. They have evaluated the influence of natural frequencies and Coriolis excitation mode on the flow

characteristics. Even though this work includes the analysis of CFM made up of tubes with pre-defined curvature, the authors ignore the curvature of the tube due to sagging. Samer et al. [12] studied the vibrational characteristics of a CFM made up of a circular tube. They used the dynamic stiffness matrix method to model the tube, and the effect of natural frequency, flow velocities, axial forces and tube responses on the dynamic characteristics of CFM is studied. Wang et al. [13] demonstrated an analytical technique to evaluate the sensitivity of the CFM using the reciprocity principle, and this model is capable of determining the sensitivity of flowmeter with any shape. They have optimized the locations of sensors attached to the U tube CFM.

Juel et al. [14] investigated the effects of support conditions, non-uniformity in the mass and stiffness of tube, non-proportional damping, non-linearity and flow imperfections on the phase shift of CFM. The governing equations for the pipes conveying are derived using Hamilton's Principle. Li et al. [15] suggested some advanced techniques in signal processing, such as sophisticated bandpass filtering and complex notch filtering. They have found that the new methods give slight delay, significant noise elimination and high accuracies for CFMs. Li et al. [16] described a new technique to evaluate the frequency and time decay of the sensor's output signals of CFM based on Lagrangian interpolation function. They proposed various signal processing techniques to boost the accuracy and computation time of CFM. Felix et al. [17] show a prism signal processing technique which facilitates fast-tracking of input and output signals of the CFM. They found that more accurate measurements result using a higher frequency resonant flow tube. Satish et al. [18] conducted the experimentations of several U tube configurations of CFM. The found that the locations of sensors, drive frequencies, length to diameter ratio, torsional stiffness influences the design parameters of CFM. Ridder et al. [19] showed the impact of external disturbances on the dynamic responses of CFM for low flow rates. They develop a numerical model from the patented design, and the characteristic is experimentally validated. They utilize a pre-defined vibration excitation for estimating the error factor.

Mole et al. [20] introduced a numerical model for the analysis of Coriolis mass flow meter using coupled finite volume method for the fluid analysis and finite element method for the structural analysis. They explore the influence of vibrational mode shapes of fluid conveying tubes and velocity profile effects on the sensitivity of flow measurements. They found that the there is a noticeable reduction in the sensitivity for straight tube Coriolis mass flow meter, when the flow changes from turbulent to laminar. Kutin and Bajsic [21] develops a shell Coriolis mass flow meter using Flugge's shell theory for developing governing equations for the structure and potential flow for the fluid. They compared the results of shell and beam mode Coriolis mass flow meter and found that the shell Coriolis mass flow meter possess higher sensitivity in flow measurements. Bobovnik et al. [22] did coupled finite element and finite volume analysis on the Coriolis mass flow meter made up of deformable shells and found that the deviation in natural frequencies predicted by shell model and Euler-Bernoulli beam model is very small while the phase difference predicted by Euler-Bernoulli beam model for shorter tube is high compared to the shell model. The Timoshenko beam model as well as Shell model gives more accurate phase differences compared to the Euler-Bernoulli beam model. Monga et al. [23] generate a micro-CFM made up of SU-8. The CFM is made up of rectangular channels and actuated by Lorentz forces. The Su-8 sensors are not superior to other sensors like silicone Coriolis flow meter due to the high damping ratios, low accuracy, lower mechanical strength and lower mechanical rigidity.

Binulal et al. [1,24] use the Principle of virtual work to develop a numerical model of a CFM made up of a flexible tube. They developed a CFM using straight Polyurethane tube and found that as the flow velocity rises, the time lag due to phase shift also increases. Clark et al. [25] investigated the flow tube dynamic response using finite element simulations and verified the results experimentally. They found that quick switching of flow control devices in the tubes results in mechanical vibrations and errors in measurements. Clark et al. [26,27], Svete et al. [28] and Cheesewright et al. [29] found that the flow pulsations in the CFM can cause the tube to excite due to 'internal' vibrations in addition to the drive motor excitation and the tube experiences an additional vibration excitation at the beat frequency. Sometimes the beat can be insignificant in measurements but imparts some errors in flow measurements in the presence of flow pulsations. Smith et al. [30] and Enoksson et al. [31] develop a micro Coriolis flowmeter made up of silicone tube. The fluid conveying microtube is excited electrostatically, and these micro CFMs is used to measure the flow rates of the range 0–0.5 g/s. The comprehensive review of the literature reveals that the Coriolis mass flow meter made up of flexible tubes is very limited, and the authors neglect the effect of sagging for the flexible tubes conveying fluid.

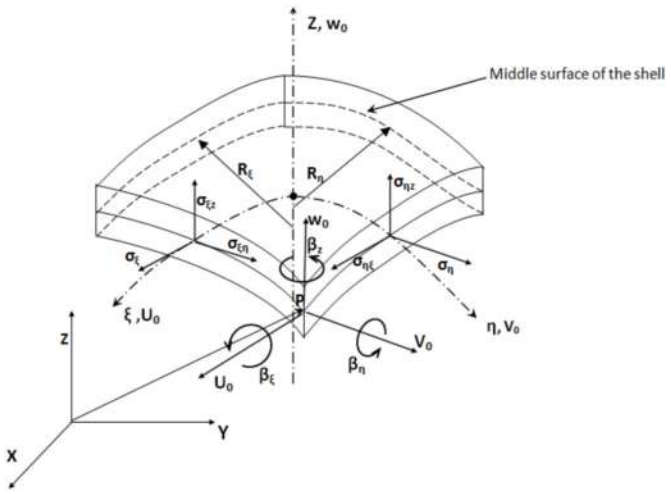


**Fig. 1.** Geometry of shell.

### 1.1. The novelty of this paper lies in

(a) The application of the numerical model of the flexible tube conveying fluid in a Coriolis mass flow meter.
(b) The numerical and experimental investigation of the influence of the beat phenomenon due to sagging in the dynamic characteristics of Coriolis mass flow meter.
(c) The identification of the difference in the meter sensitivities concerning the straight cylindrical tube and actual sagged flexible tube.
(d) The estimation of the causes and remedies for the non-linearities in the calibration curves of Coriolis mass flow meter.

## 2. Theory

### 2.1. Governing equations for modelling of shells [5,32,33–38]

In the Mindlin shell theory, the mid plane displacements are defined in terms of the shell thickness and the rotations of a plane cross-section are not related to the derivatives of the transverse displacements. The normal strains acting on the plane parallel to the middle surface are negligible compared with the other strain components. Fig. 1 shows the geometry of mindlin shell.

Assumptions made in the derivation of shell theory are.

(a) The shell material is isotropic.
(b) Deflections are small compared with shell thickness.
(c) Neglect the shell gravity forces.
(d) The change in the thickness of the shell due to pre-stretching is neglected.

(e) Normals to the mid surface strains remain straight during deformation but not normal to the surface.

The displacements of a point in the shell at a distance 'z' above the centroidal plane can be given as

$$u(\xi,\eta,z) = u_0(\xi,\eta) + z\,\beta_x\,(\xi,\eta) \tag{1}$$

$$v(\xi,\eta,z) = v_0(\xi,\eta) - z\,\beta_y\,(\xi,\eta) \tag{2}$$

$$w(\xi,\eta) = w_0(\xi,\eta) \tag{3}$$

The strains at any point can be written as:

$$\varepsilon_\xi = \frac{1}{\left(1+\frac{z}{R_\xi}\right)}(\varepsilon_{0\xi} + zK_\xi) \tag{4}$$

$$\varepsilon_\eta = \frac{1}{\left(1+\frac{z}{R_\eta}\right)}(\varepsilon_{0\eta} + zK_\eta) \tag{5}$$

$$\gamma_{\xi\eta} = \frac{1}{\left(1+\frac{z}{R_\xi}\right)}(\gamma_{0\xi\eta} + zK_{\xi\eta}) \tag{6}$$

$$\gamma_{\eta z} = \frac{1}{\left(1+\frac{z}{R_\eta}\right)}\left(\gamma_{0\xi\eta} + z\frac{\beta_\eta}{R_\eta}\right) \tag{7}$$

$$\gamma_{z\xi} = \frac{1}{\left(1+\frac{z}{R_\xi}\right)}\left(\gamma_{0z\xi} + z\frac{\beta_\xi}{R_\xi}\right) \tag{8}$$

where the mid surface strains can be written in terms of mid surface displacements, radius of.

The radius of curvatures and the twist changes can be evaluated as

$$K_\xi = \frac{1}{A}\frac{\partial\beta_\xi}{\partial\xi} + \frac{\beta_\eta}{AB}\frac{\partial A}{\partial\eta} \tag{9}$$

$$K_\eta = \frac{1}{B}\frac{\partial\beta_\eta}{\partial\eta} + \frac{\beta_\xi}{AB}\frac{\partial B}{\partial\xi} \tag{10}$$

$$K_{\xi\eta} = \frac{1}{A}\frac{\partial\beta_\eta}{\partial\xi} - \frac{\beta_\xi}{AB}\frac{\partial A}{\partial\eta} \tag{11}$$

The lames parameters of the shell element in the local curvilinear coordinate system $(\xi,\eta)$ can be expressed in terms of the Cartesian coordinates (x, y, z) as

$$A^2 = \left(\frac{\partial x}{\partial\xi}\right)^2 + \left(\frac{\partial y}{\partial\xi}\right)^2 + \left(\frac{\partial z}{\partial\xi}\right)^2 \tag{12}$$

$$B^2 = \left(\frac{\partial x}{\partial\eta}\right)^2 + \left(\frac{\partial y}{\partial\eta}\right)^2 + \left(\frac{\partial z}{\partial\eta}\right)^2 \tag{13}$$

Using the relations, we can write the strain displacement relation in the form

$$\{\varepsilon\} = [B_s]\{U_e\} \tag{14}$$

where $[B_s]$ is the shell strain displacement matrix.

The elemental stress can be evaluated using the stress strain relationship as

$$\{\sigma\} = [D_s]\{\varepsilon\} \tag{15}$$

where the constitutive relation matrix $[D_s]$ for an isotropic material is given as

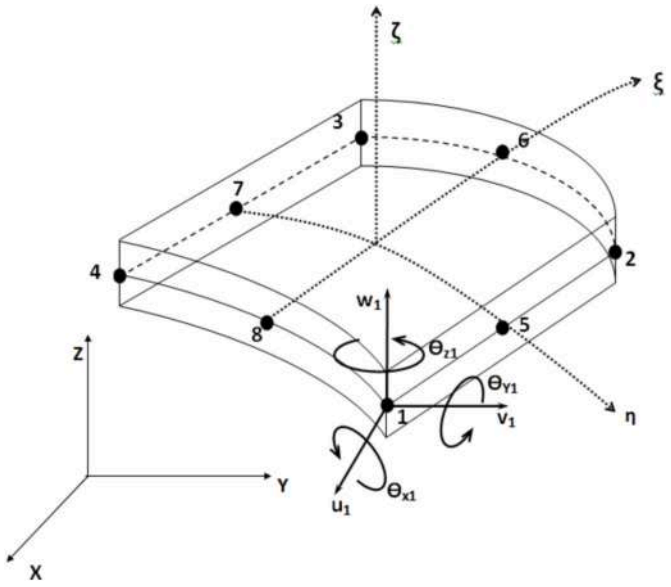


**Fig. 2.** Eight noded Mindlin shell element.

$$[D_s] = \frac{E}{(1+\vartheta)(1-2\vartheta)}\begin{bmatrix} 1-\vartheta & \vartheta & \vartheta & 0 & 0 & 0 \\ \vartheta & 1-\vartheta & \vartheta & 0 & 0 & 0 \\ \vartheta & \vartheta & 1-\vartheta & 0 & 0 & 0 \\ 0 & 0 & 0 & \frac{1-2\vartheta}{2} & 0 & 0 \\ 0 & 0 & 0 & 0 & \frac{1-2\vartheta}{2} & 0 \\ 0 & 0 & 0 & 0 & 0 & \frac{1-2\vartheta}{2} \end{bmatrix} \tag{16}$$

### 2.2. Finite element formulation of shells

The pipe structure is discretized into many number eight noded Mindlin shell elements with different orientations. Fig. 2 shows the geometry of eight noded isoparametric shell element. The plane stress component in the normal direction of the shell structure is assumed to be zero. Six degrees of freedoms have been defined for each elemental node, three translations, and three rotations in the global XYZ direction. The rotation along the z-axis is commonly known as the drilling degree of freedom, which is added to the node to bypass the ill condition of the assembled global stiffness matrix [36,38]. The generalized global displacement vector for an 'ith' node of 8 noded shell element can be expressed as

$$U_{ei} = \begin{Bmatrix} U_i \\ V_i \\ W_i \\ \theta_{xi} \\ \theta_{yi} \\ \theta_{zi} \end{Bmatrix} \tag{17}$$

*The displacement at any point can be expressed as*

$$\begin{Bmatrix} U_i \\ V_i \\ W_i \\ \theta_{xi} \\ \theta_{yi} \\ \theta_{zi} \end{Bmatrix} = \begin{Bmatrix} N_1 & 0 & N_2 & 0..... & N_8 \\ 0 & N_1 & 0 & N_2..... & N_8 \end{Bmatrix} \begin{Bmatrix} U_1 \\ V_1 \\ . \\ . \\ \theta_{y8} \\ \theta_{z8} \end{Bmatrix} \tag{18}$$

where $N_1$ to $N_8$ represents the shape functions which are defined as

$$For\ \ corner\ \ nodes\ \ N_i = \frac{1}{4}(1+\xi_a\xi)(1+\eta_a\eta)(\xi_a\xi+\eta_a\eta-1) \tag{19}$$

$$For\ \ mid-size\ \ nodes\ \ \xi_a = 0;\ N_i = \frac{1}{2}(1-\xi^2)(1-\eta_a\eta) \tag{20}$$

$$For\ \ mid-size\ \ nodes\ \ \eta_a = 0;\ N_i = \frac{1}{2}(1-\xi_a\xi)(1-\eta^2) \tag{21}$$

Using the shell strain displacement matrix the Stiffness matrix of the shell can be evaluated as

$$K_s = \Delta B_s D_s B_s^T dv \tag{22}$$

The integration of the above equation is carried out using Gauss Quadrature technique of numerical integration.

### 2.3. Geometric stiffness updation to incorporate pre-stretching [39]

The pre-stretching can cause the stiffness to increase along the longitudinal direction of the shell. This increase in stiffness can be evaluated by conducting static analysis of the shell. The nodal displacements can be used to evaluate the elemental strains and stresses acting on the Mindlin shell.

The geometric stiffness $K_g$ can be found out using the equation

$$K_g = \iint B_m^T \sigma_{ij} B_m dA \tag{23}$$

where

$$\sigma_{ij} = \begin{bmatrix} \sigma_{xx} & \tau_{xy} & \tau_{xz} \\ \tau_{yx} & \sigma_{yy} & \tau_{yz} \\ \tau_{zx} & \tau_{zy} & \sigma_{zz} \end{bmatrix} \tag{24}$$

The geometric stiffness is added to the membrane stiffness to get the total longitudinal stiffness. Hence the total stiffness of the shell can be written as $K = K_s + K_g$

### 2.4. Mindlin shell mass matrix [40]

To obtain the mass matrix for curved Mindlin shell, we adopt the same technique used for deriving stiffness matrix. The mass matrix of the two-dimensional solid element is used for accounting the in-plane loading effect, and the 2D plate element formulation is applied for deriving the bending effect.

From the relation of Kinetic energy of shells, we can derive the mass matrix of the shell as

$$The\ \ kinetic\ \ energy\ \ of\ \ shell\ \ Ke = \frac{1}{2}\int \dot{U}^T m \dot{U} dV \tag{25}$$

Hence the mass matrix can be obtained from the shell shape functions as

$$m = \Delta\rho N^T N dV \tag{26}$$

Numerical integration using Gauss Quadrature is used to evaluate the integral.

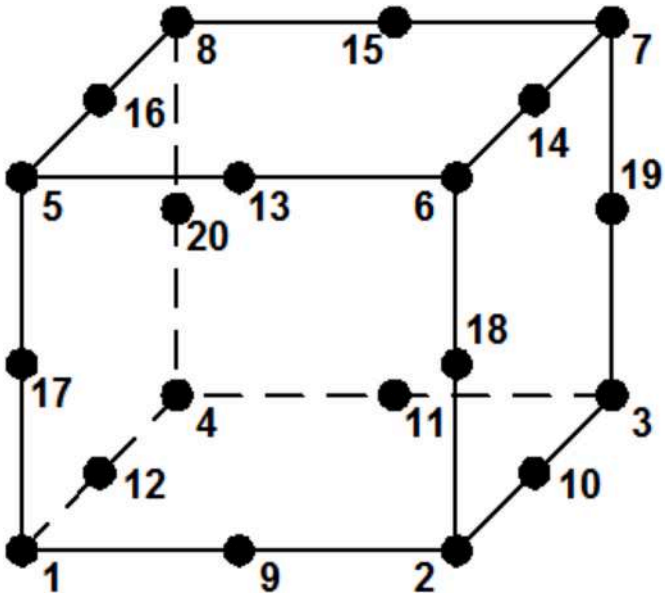


**Fig. 3.** Geometry of Twenty noded fluid element.

### 2.5. Transformation Matrix [41]

The stiffness and mass matrices of shell elements are evaluated with reference to the natural coordinate system, and it has to be transformed into the global coordinate system using the transformation matrix.

The nodal displacements and rotations of the shell can be expressed using transformation matrix as

$$\begin{Bmatrix} d_1 \\ d_2 \\ d_3 \\ d_4 \\ d_5 \\ d_6 \end{Bmatrix} = \begin{bmatrix} H & 0 \\ 0 & H \end{bmatrix} \begin{Bmatrix} u_1 \\ v_1 \\ w_1 \\ \theta_{1x} \\ \theta_{1y} \\ \theta_{1z} \end{Bmatrix} \tag{27}$$

The components of this transformation matrix are the cosines of the angles between the three-elemental local axes.

$$\begin{Bmatrix} \xi \\ \eta \\ \zeta \end{Bmatrix} = \begin{Bmatrix} l_\xi & m_\xi & n_\xi \\ l_\eta & m_\eta & n_\eta \\ l_\zeta & m_\zeta & n_\zeta \end{Bmatrix} \begin{Bmatrix} x \\ y \\ z \end{Bmatrix} \tag{28}$$

$$H = \begin{Bmatrix} l_\xi & m_\xi & n_\xi \\ l_\eta & m_\eta & n_\eta \\ l_\zeta & m_\zeta & n_\zeta \end{Bmatrix} \tag{29}$$

### 2.6. Finite element modelling of acoustic fluid element [5,32,42,43]

Twenty noded isoparametric elements are used in the finite element formulation of the fluid domain. The geometry of fluid element is shown in Fig. 3. The wave equation describes the phenomenon of flow as the energy is propagated by the wave. The potential is taken as the nodal DOF for the element formulation of the wave equation. Nodal DOF for the acoustic fluid element is taken as three.

The assumptions made in developing the finite element equations for the fluid region.

(1) The fluid flow is due to the potential and plug flow.
(2) Flow is compressible in nature, irrotational, isentropic, and inviscid.
(3) The fluid pressure always acts normal to the shell wall,
(4) Flow separation, or cavitation does not take place.

The velocity potential satisfies the wave equation as given below:

$$\nabla^2\varphi - \frac{1}{C^2}\left(\frac{\partial}{\partial t} + U_z\frac{\partial}{\partial z}\right)\varphi = 0 \tag{30}$$

The radial and axial velocity of flow can be expressed as

$$V_r = \frac{\partial\varphi}{\partial r}\ ,\ V_z = U_z + \frac{\partial\varphi}{\partial z} \tag{31}$$

To satisfy the impermeability between fluid and structure, we assume the radial fluid velocity to be equal to the shell velocity in the same direction. This boundary condition assures proper connection between fluid and shell.

Therefore the velocity of the shell can be given as

$$V_r = \left(\frac{\partial\varphi}{\partial r}\right)_{r=R} = \frac{\partial w}{\partial t} + U_z\frac{\partial w}{\partial x} \tag{32}$$

The Bernoulli's equation helps to obtain the pressure exerting on the shell surface which states as

$$\frac{\partial\varphi}{\partial t} + \frac{1}{2}V^2 + \frac{P_p}{\rho} = \frac{P_s}{\rho} \tag{33}$$

where

$$V^2 = V_z^2 + V_\theta^2 + V_r^2 \tag{34}$$

and

$$P_p = \overline{P} + p \tag{35}$$

The higher order terms in $V^2$ are ignored, and hence we get $V^2 \cong U_z^2 + 2U_z\frac{\partial\varphi}{\partial x}$

$$P_p = -\rho\left(\frac{\partial\varphi}{\partial t} + U_z\frac{\partial\varphi}{\partial x}\right) \tag{36}$$

The finite element equations of the fluid flow (wave equation) can be formulated using the Galerkin weighted residual method with the potential as the weighting function. The equation can be written as

$$\int_V N_f^T\left(\nabla^2\varphi - \frac{1}{C^2}\left(\frac{\partial}{\partial t} + U_z\frac{\partial}{\partial z}\right)^2\varphi\right)dV = 0 \tag{37}$$

$$\int_S N_f^T\nabla\varphi.ndS - \int_V \nabla N_f^T\nabla\varphi dV - \frac{1}{C^2}\int_V N_f^T\ddot{\varphi}dV - \frac{2U_z}{C^2}\int_V N_f^T\frac{\partial^2\varphi}{\partial z\partial t}dV - \frac{U_z^2}{C^2}\int_V N_f^T\frac{\partial^2\varphi}{\partial z^2}dV = 0 \tag{38}$$

where the fluid shape functions $N_f$is given by

$$For\ the\ corner\ nodes\ N_i = \frac{1}{8}(1+\xi_i\xi)(1+\eta_i\eta)(1+\varsigma_i\varsigma)(\xi_i\xi+\eta_i\eta+\varsigma_i\varsigma-2) \tag{39}$$

For mid side edge nodes $\xi_i = 0;\ \eta_i = \pm 1\ ;\ \varsigma_i = \pm 1$

$$N_i = \frac{1}{4}(1-\xi^2)(1+\eta_i\eta)(1+\varsigma_i\varsigma) \tag{40}$$

The first term of the equation is rewritten by applying the boundary conditions as

$$\int_S N_f^T\nabla\varphi.ndS = \int N_f^T\overline{N}dS\left\{\dot{U}_e\right\} + U_z\int N_f^T\frac{\partial\overline{N}}{\partial z}dS\{U_e\} \tag{41}$$

where $\overline{N}_s$ represents the shell shape function component along Z direction, and 'n' is the normal unit vector to the shell.

The finite element equation of fluid domain considering the pressure acting on the surface can be expressed as

$$\int_S \overline{N}_s{}^T\rho_f\left(\frac{\partial\varphi}{\partial t} + U_z\frac{\partial\varphi}{\partial z}\right)dS = \rho_f\int_S \overline{N}_s{}^T N_f dS\left\{\dot{\varphi}_e\right\} + \rho_f U_z\int_S \overline{N}_s{}^T\frac{\partial N_f}{\partial z}dS\{\varphi_e\} \tag{42}$$

Combining both the equations, the complete fluid-structure interaction equation for the structure and acoustic fluid can be expressed as

$$\begin{bmatrix} M_s^{uu} & 0 \\ 0 & G_f^{\varphi\varphi} \end{bmatrix}\begin{Bmatrix}\ddot{u}\\ \ddot{\varphi}\end{Bmatrix} + \begin{bmatrix} 0 & C_{fs}^{u\varphi} \\ -C_{fs}^{\varphi u} & -U_z G_{fs}^{\varphi\varphi}\end{bmatrix}\begin{Bmatrix}\dot{u}\\ \dot{\varphi}\end{Bmatrix} + \begin{bmatrix} K_s^{uu} & U_x K_{fs}^{u\varphi} \\ -U_z K_{fs}^{\varphi u} & H_f^{\varphi\varphi} - U_z^2 I_f^{\varphi\varphi}\end{bmatrix}\begin{Bmatrix} u\\ \varphi\end{Bmatrix} = 0 \tag{43}$$

where

$$Elemental\ mass\ matrix, m_{es} = \rho_s\int N_s^T N_s\ dV$$

$$Structural\ mass\ matrix,\ M_s^{uu} = \sum m_{es}$$

$$Elemental\ fluid\ compression\ energy, G_{ef}^{\varphi\varphi} = \frac{1}{c^2}\int N_f^T N_f\ dV$$

$$Structural\ Fluid\ compression\ energy,\ G_f^{\varphi\varphi} = \sum G_{ef}^{\varphi\varphi}$$

$$\text{Elemental Fluid Structure interaction coupling term, } C_{efs}^{u\varphi} = \rho_f\int \overline{N}_s^T N_f\ dS$$

$$Fluid\ Structure\ \text{interaction coupling term},\ C_{fs}^{u\varphi} = \sum C_{efs}^{u\varphi}$$

$$\text{Elemental Fluid Structure interaction coupling term, } C_{efs}^{\varphi u} = \int N_f^T\overline{N}_s\ dS$$

$$Fluid\ Structure\ \text{interaction coupling term}, C_{fs}^{\varphi u} = \sum C_{efs}^{\varphi u}$$

$$Elemental\ Coriolis\ energy\ of\ fluid,\ C_{ef}^{\varphi\varphi} = \frac{2U_z}{c^2}\int N_f^T\frac{\partial N_f}{\partial x}dV$$

$$Coriolis\ energy\ of\ Fluid,\ C_f^{\varphi\varphi} = \sum C_{ef}^{\varphi\varphi}$$

$$Elemental\ Stiffness\ matrix\ of\ shell, K_{es}^{uu} = \int B^T DB\ dV$$

$$Structural\ Stiffness\ matrix, K_s^{uu} = \sum K_{es}^{uu}$$

$$Elemental\ Stiffness\ coupling\ due\ to\ flow,\ K_{efs}^{u\varphi} = \rho_f\int \overline{N}_s^T\frac{\partial N_f}{\partial x}dS$$

$$Stiffness\ coupling\ due\ to\ flow,\ K_{fs}^{u\varphi} = \sum K_{efs}^{u\varphi}$$

$$Elemental\ Stiffness\ coupling\ due\ to\ flow,\ K_{efs}^{\varphi u} = \rho_f\int \overline{N}_f^T\frac{\partial N_s}{\partial x}dS$$

$$Stiffness\ coupling\ due\ to\ flow,\ K_{fs}^{\varphi u} = \sum K_{efs}^{\varphi u}$$

$$Elemental\ Kinetic\ energy\ of\ fluid,\ H_{ef}^{\varphi\varphi} = \int \nabla N_f^T\nabla N_f dV$$

$$Kinetic\ energy\ of\ fluid,\ H_f^{\varphi\varphi} = \sum H_{ef}^{\varphi\varphi}$$

$$Elemental\ Centrifugal\ Energy\ of\ fluid,\ I_{ef}^{\varphi\varphi} = \frac{U_z^2}{c^2}\int\frac{\partial N_f^T}{\partial x}\frac{\partial N_f}{\partial x}dV$$

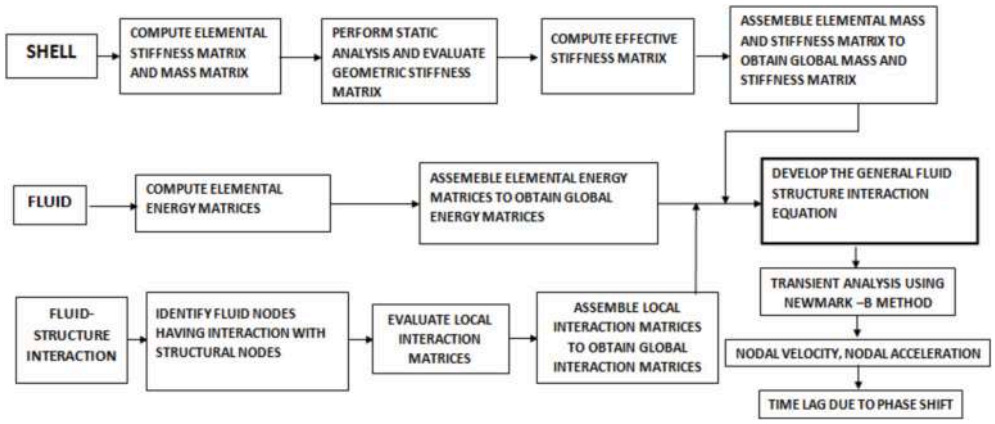


**Fig. 4.** Flow chart describing the numerical analysis.

*Centrifugal Energy of fluid,* $I_f^{\varphi\varphi} = \sum I_{cf}^{\varphi\varphi}$

The general fluid-structure interaction equation is then assembled using the structural stiffness matrices, structural mass matrices, fluid energy matrices and the coupling matrices. This general fluid-structure interaction equation is generally an Eigen value problem; hence the solution gives Eigen values and Eigen vectors. These Eigen values give the natural frequencies of the system, while Eigen vector helps to plot the corresponding mode shapes.

### 2.7. Numerical integration using Newmark- β method [44]

The solution for transient fluid-structure interaction problem is obtained using the Newmark-β method of numerical integration. Fig. 4 represents the flow chart for the numerical analysis of Coriolis mass flow meter. The nodal displacement, velocity and acceleration of the structure are computed from the incremental equations of equilibrium. The technique involves step-by-step integration in which the solution for nodal variables is obtained from one-time step to the next time step. For every small time step (denoted as Δt), the equation of motion for time step $t_{n+1}$ in terms of nodal displacement, velocity and acceleration can be found out using the following relations.

$$x_{n+1} = x_n + \Delta t\dot{x}_n + (0.5-\beta)(\Delta t)^2\ddot{x}_n + \beta(\Delta t)^2\ddot{x}_{n+1} \tag{44}$$

$$\dot{x}_{n+1} = \dot{x}_n + (1-\gamma)\Delta t\ddot{x}_n + \gamma\Delta t\ddot{x}_{n+1} \tag{45}$$

For γ = 0.5, we get the relations for velocity and acceleration as

$$\dot{x}_{n+1} = \dot{x}_n + \left(\frac{\Delta t}{2}\right)\left(\ddot{x}_n + \ddot{x}_{n+1}\right) \tag{46}$$

$$\ddot{x}_{n+1} = \frac{1}{m}\left[P_{n+1} - c\dot{x}_{n+1} - kx_{n+1}\right] \tag{47}$$

The parameters β and γ are selected suitably based on the accuracy and stability criteria. For each time step, the values of β and γ are taken as $\beta \geq 0.5$and $\gamma \geq 0.25(0.5+\beta)^2$.

The equation of motion, at any time, t+1, can be specified as:

$$[M]\left\{\ddot{x}_{t+1}\right\} + [C]\left\{\dot{x}_{t+1}\right\} + [K]\{x_{t+1}\} = \{P_{n+1}\} \tag{48}$$

The iteration starts with an assumed values for the initial displacement and velocity at time, t = 0. Using the structural, fluidic and interaction modules, the mass matrix [M], the stiffness matrix, [K] and damping matrix, [C] are computed as

$$[M] = \begin{bmatrix} M_s^{uu} & 0 \\ 0 & G_f^{\varphi\varphi} \end{bmatrix}$$

$$[C] = \begin{bmatrix} 0 & C_{fs}^{u\varphi} \\ -C_{fs}^{\varphi u} & -U_z G_{fs}^{\varphi\varphi} \end{bmatrix}$$

$$[K] = \begin{bmatrix} K_s^{uu} & U_x K_{fs}^{u\varphi} \\ -U_z K_{fs}^{\varphi u} & H_f^{\varphi\varphi} - U_z^2 I_f^{\varphi\varphi} \end{bmatrix}$$

The constants used in the integration are found out using the relations

$$a_0 = \frac{1}{\beta(\Delta t)^2};\ a_1 = \frac{\gamma}{\beta\Delta t};\ a_2 = \frac{1}{\beta\Delta t};\ a_3 = \frac{1}{2\beta} - 1$$

$$a_4 = \frac{\gamma}{\beta} - 1; a_5 = \frac{\Delta t}{2}\left[\frac{\gamma}{\beta} - 2\right]; a_6 = \Delta t(1-\gamma);\ a_7 = \gamma\Delta t$$

For every time step the integration equation is solved to find the effective stiffness matrix and hence the corresponding effective force, nodal velocity and acceleration are found out. The initial acceleration is evaluated from equation (48) for a time step at t = n. Assume a value of acceleration at time step n+1. Solve for new acceleration at time 'n+1' using equation (48). We define suitable convergence criteria to compare the acceleration at time steps 'n+1' and 'n'. If the required condition is not met, the acceleration at time step 'n+1' will get revised.

The effective stiffness matrix can be given as,

$$\left[\widehat{K}\right] = [K] + a_0[M] + a_1[C] \tag{49}$$

And the effective force,

$$\left\{\widehat{P}_{n+1}\right\} = \{P_{n+1}\} + [M]\left(a_0\{x_n\} + a_2\left\{\dot{x}_n\right\} + a_3\left\{\ddot{x}_n\right\}\right) + [C]\left(a_1\{x_n\} + a_4\left\{\dot{x}_n\right\} + a_5\left\{\ddot{x}_n\right\}\right) \tag{50}$$

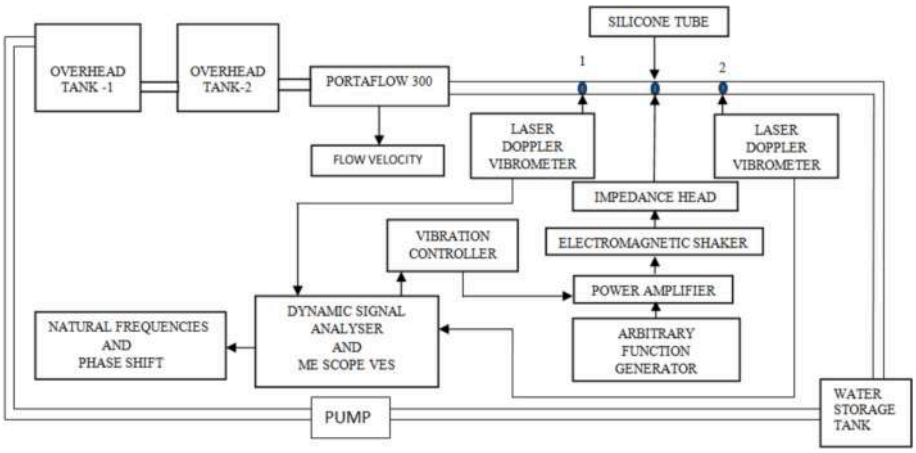


**Fig. 5.** Layout of the experimentation setup.

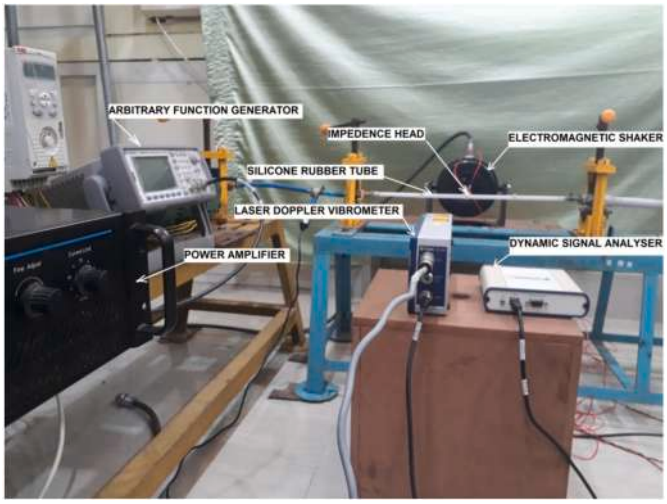


**Fig. 6.** Experimentation setup arrangement.

**Table 1**
Parameters of silicone tube.

| Tube material | Silicone rubber |
|---|---|
| Tube dimensions | Inner diameter = 0.006 m<br>Outer diameter = 0.009 m |
| Material properties of silicone polymer | Modulus of Elasticity, E = 5 MPa<br>Material density, $\rho = 1100$ kg/m$^3$ |
| End conditions of tube | Both ends clamped |

The nodal displacement can be found out from the effective force as

$$\left[\widehat{K}\right]\{x_{n+1}\} = \left\{\widehat{P}_{n+1}\right\} \tag{51}$$

The acceleration and velocity can be found as

$$Acceleration, \left\{\ddot{x}_{n+1}\right\} = a_0(\{x_{n+1}\} - \{x_n\}) - a_2\left\{\dot{x}_n\right\} - a_3\left\{\ddot{x}_n\right\} \tag{52}$$

$$Velocity\left\{\dot{x}_{n+1}\right\} = \left\{\dot{x}_n\right\} + a_6\left\{\ddot{x}_n\right\} + a_7\left\{\ddot{x}_{n+1}\right\} \tag{53}$$

The sinusoidal excitation (with constant frequency) is given at a node located at the center of fluid conveying tube in the finite element model of Coriolis mass flow meter. The nodal velocity responses of two equidistance nodes from the point of excitation are acquired. The responses show a phase shift, which is proportional to the mass flow rate of conveying fluid.

## 3. Experimentation

Designed an experimental setup for investigating the vibrational performance of silicone tubes with the steady-state flow condition, and Fig. 5 shows the layout of the experimental setup. Care is taken to avoid resonance by keeping the combined frequency of frame and test structure over 120 Hz. The experiments were carried out in a closed-circuit system with recirculating water. The test setup consists of clamped-clamped horizontally placed silicone tube (with arrangement for pre-stretching), three water storage tanks, controllers, actuators and response sensors. Fig. 6 shows the experimentation setup used for the analysis of Coriolis mass flow meter. Two storage tanks with interconnecting pipes and float valve are used to maintain constant head over the silicone tube and to reduce the undulations in fluid flow. The fluid passing the test section is collected at tank 3 and it is given back to tank 1 using a pump. The silicone rubber tube is excited at its fundamental frequency using the electromagnetic shaker. The properties of silicone rubber tube are given in Table 1. A function generator (Tektronix AFG3022B) generates the input sine wave signal for electromagnetic shaker and the generated signal is amplified with the help of a power amplifier (Sentek Dynamics LA 300, rated output-300 VA).

A stinger rod is attached on the electromagnetic shaker and force transducer (Dytran, 22.5 mV/N) is attached at the free end of the stinger, the center of the fluid conveying tube is fixed firmly to the force transducer. The response of the fluid conveying tube is examined using the roving output method, where the tube is always excited at its centre. An ultrasonic flow meter (Portaflow 300, Micronics Ltd, with the velocity limit of 0.05–15 m/s) is used to measure the flow velocity. The dynamic responses of two equidistant points from the excitation are acquired using the laser Doppler vibrometer (Polytec IVS400). The impedance head signal (excitation force) and the response (tube vibration velocity from vibrometer) were gathered employing the Dynamic Signal Analyzer (DSA). ME'scope VES analysis software is used for the processing of input and output signals.

Generally, in Coriolis mass flow meter the tube is continuously excited at its fundamental frequency to minimise the energy required for

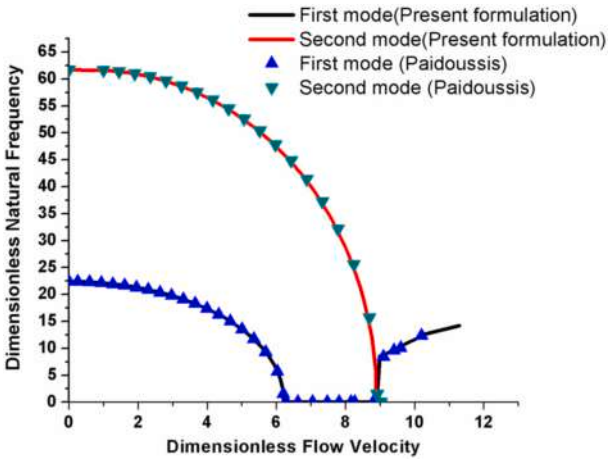


**Fig. 7.** Comparison of the MATLAB program with the results of Païdoussis.

**Table 2**
First fundamental frequency of 36 cm long empty tube under different pre-stretches.

| Sl no | Length of Tube | Experimental frequency (Hz) | Numerical frequency (Hz) | Difference (%) |
|---|---|---|---|---|
| 1 | 32.4 cm + 3.6 cm (Pre Stretch) | 24.3 | 24.416 | 0.47 |
| 2 | 30.6 cm + 5.4 cm (Pre Stretch) | 29.3 | 29.436 | 0.46 |
| 3 | 28.8 cm + 7.2 cm (Pre Stretch) | 30.1 | 30.229 | 0.42 |

excitation. Thus the excitation at fundamental frequency will cause resonance, which leads to increase in amplitude of vibration [45]. Since the tube is flexible, the oscillations may become uncontrollable after some time. The amplitude of vibration is limited by means of Notching technique using a Vibration controller (Rula Technologies, RL-C21). Here the limit of vibration is assigned as ± 3 mm. RL-C21 helps in attaining is a closed loop control system, which limits the oscillations to the prescribed values. The level of vibrations is monitored using the responses received from the laser Doppler vibrometer and based on the predefined limit of vibration; the vibration controller will control the amplitude of vibration through the power amplifier and hence the drive amplitude will be reduced during the resonance condition.

Different combinations of parameters such as the number of samples, sampling frequency, excitation duration, and hold time of the excitation waveform are tried out, and the values for the signal processing are found out. The sampling rate is taken as 8192 samples for the time duration of 6.55 s. The excitation signal application time is taken as 7 s and a pause time of 2 s. The Hanning window is used for signal conditioning [46,47].

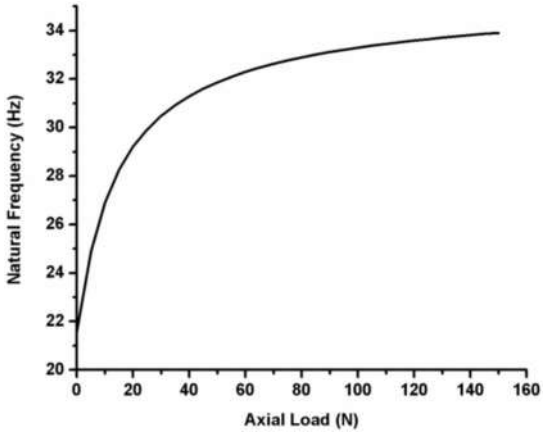


**Fig. 9.** Natural frequency Vs axial load for a 36 cm long tube.

The fluid conveying tube is excited at its centres using a sinusoidal signal of constant frequency. The signal is generated using an arbitrary function generator, and then the signal is amplified using power amplifier. The frequency of excitation remains the same, and the response from two equi-distance point of excitation is obtained with the help of laser Doppler vibrometer. The time lag can be obtained from the temporal shift measured along the time axis, between the zero crossing points of the time-response curves. A Matlab program is developed to identify the zero crossing points of the velocity curves.

## 4. Results and discussion

### 4.1. Numerical validation of program with results available in literature [48]

The Mindlin shell finite element model for tube conveying fluid is validated, employing the results presented by Païdoussis [48]. He examined the flow-induced vibrations and instabilities of cylindrical structures conveying incompressible, isentropic, and inviscid fluid. Fig. 7 shows the variation of the dimensionless flow velocity, u versus the dimensionless natural frequency $\omega/\omega_o$ for the clamped-clamped pipes with β as 0.1. Here β represents the mass ratio (the ratio of the fluid mass to the sum of structural and the fluid masses), ω is the frequency of the structure, $\omega_o$ is $\sqrt{EI/(m+M)L^4}$ and u is $\sqrt{\left(EI/ML^2\right)}U_z$ where $U_z$ is the flow velocity, $m$ is mass per unit length of pipe, $M$ is the mass per unit length of fluid and $L$ is the length of pipe. For the zero dimensionless flow velocity of the clamped-clamped tube, the first two fundamental dimensionless natural frequencies are found to be 22.37 Hz and 61.68 Hz. As the velocity of fluid rises, the dimensionless frequency declines, and at a velocity of 2π, the first fundamental mode frequency vanishes. For a non-dimensional flow velocity of 8.99, the second

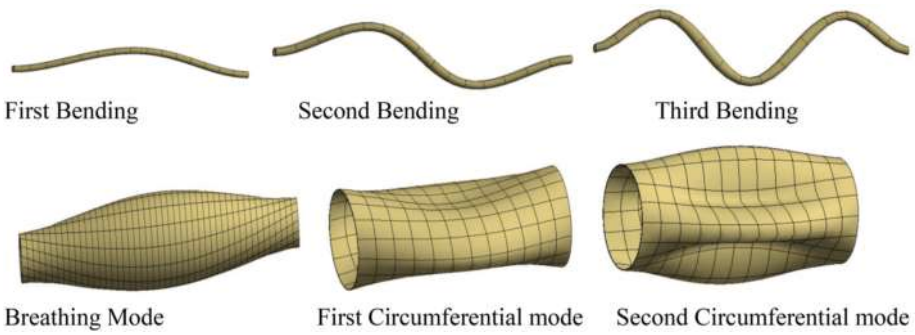


**Fig. 8.** Modes of Vibration in Shells tubes conveying fluid.

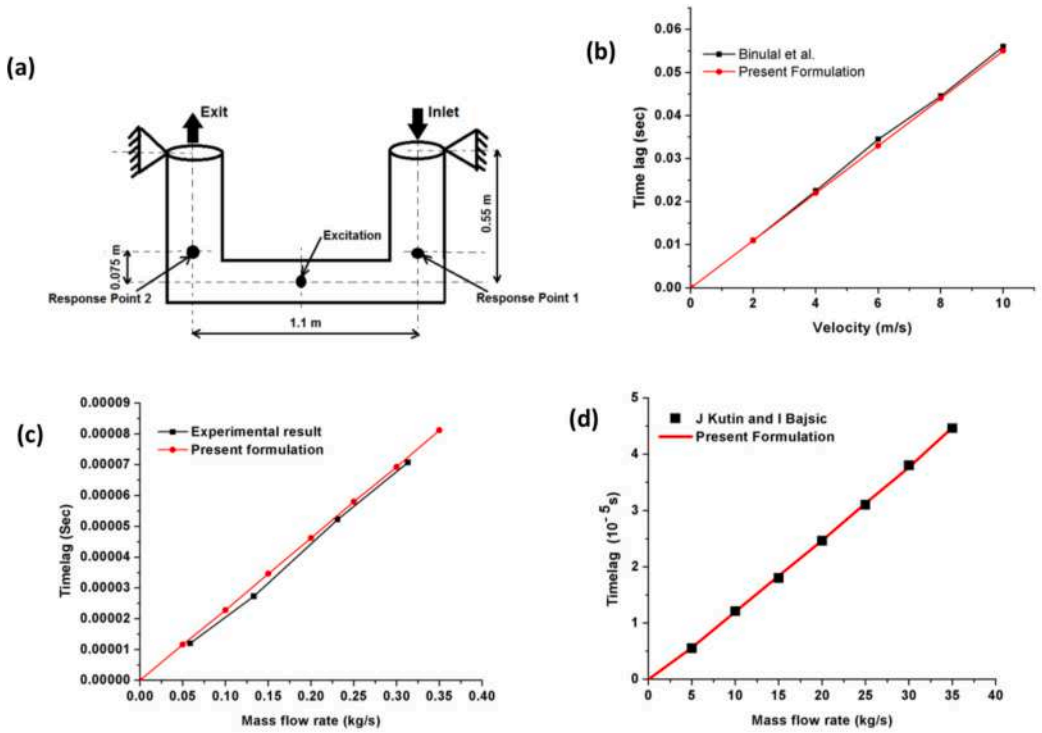


**Fig. 10.** (a) Geometry used by Binulal et al. [1] (b) Validation of Program with numerical results of Binulal et al. [1] (c) Validation of Program with experimental results of Sharma et al. [18] (d)Validation of Program with Shell model proposed by Kutin et al. [21].

**Table 3**
Properties of U tube and conveying fluid [18].

| Length of tube | 0.15 m |
|---|---|
| Distance between sensors | 0.075 m |
| Inner radius of pipe | 10 mm |
| Pipe Thickness | 0.5 mm |
| Young's Modulus of pipe | 110 GPa |
| Poisson's ratio | 0.3 |
| Density of Fluid | 1000 kg/m$^3$ |
| Density of pipe | 4500 kg/m$^3$ |
| Boundary conditions | Both ends clamped |

**Table 4**
Properties of Straight tube [21].

| Tube material | Copper |
|---|---|
| Length of tube | 0.2 m |
| Distance between two limbs | 0.5 m |
| Internal diameter of tube | 10.9 mm |
| Outer diameter of tube | 12.7 mm |
| Young's Modulus of Copper | 110 GPa |
| Poisson's ratio | 0.3 |
| Sensor location (from base) | 7.5 cm |
| Working fluid | Water |
| Density of Fluid | 1000 kg/m$^3$ |
| Boundary conditions | Both ends are fixed |
| Drive frequency | 35 Hz |

fundamental mode frequency also vanishes. From Fig. 7, it is clear that the results obtained from the present formulation agree with the results of Païdoussis.

### 4.2. *Influence of pre-stretch in the natural frequency of flexible tube*

The influence of pre-stretch on the fundamental frequency of the shell (empty tube) is identified numerically and validated with experiments. The flexible silicone tube with original length of 36 cm is analysed numerically for different pre-stretches. Table 2 shows the comparison of the first fundamental frequency of the silicone tube evaluated experimentally and numerically. The difference in the first fundamental frequency for a 36 cm long silicone tube found out numerically and experimentally is less than 1%.

The change of natural frequency with the pre-stretch for a 36 cm long empty tube is identified numerically. The mode shapes are plotted in the Matlab to identify the fundamental modes of vibration. The different modes of vibration are shown in Fig. 8. Fig. 9 displays the change in natural frequency corresponding to the pre-stretching for the shell in the absence of fluid. Initially, the change in natural frequency due to pre-stretching is more, and later the difference reduces. This shows a stabilization effect after some pre-stretching. This effect is due to the fact that elastomers like silicone rubber tubes are composed of cross-linked molecular chains that are highly twisted, kinked, and coiled. The molecular chains of these silicone rubber polymers partially uncoil when the tube is stretched along its length direction. Hence the geometric stiffness of the silicon tube gets increased [49].

First Bending Second Bending Third Bending.

Breathing Mode First Circumferential mode Second Circumferential mode.

### 4.3Validation of numerical program

The Matlab program developed for CFM analysis is validated using the numerical and experimental results available in the literature. Fig. 10 (a) shows the geometry for the numerical analysis and fig 10 (b) shows the comparison of the results from the current shell formulation and the results presented by Binulal et al. [1]. A U- tube CFM is considered for the analysis and the modelling of structure is made using Timoshenko Beam elements. The tube material used for the analysis is PVC with density as 1440 kg/m$^3$ and modulus of Elasticity as 3.3 GPa. The internal diameter and external diameter is taken as 0.019 m and 0.016 m respectively. The length of pipe is 0.55 m and the distance of

**Table 5**
Experimental evaluation of First fundamental Frequency of 25 cm long tube with fluid.

| Sl no | Pre-Stretch (%) | First Natural Frequency (Hz) | | Difference in frequency (Hz) |
|---|---|---|---|---|
| | | X-Z Plane | X–Y Plane | |
| 1 | 5 | 21.6 | 25.8 | 4.2 |
| 2 | 10 | 24.3 | 26.0 | 1.7 |
| 3 | 15 | 25.8 | 26.3 | 0.5 |
| 4 | 20 | 26.8 | 26.7 | 0.1 |

separation is 1.1 m. The tube is excited at a frequency of 14.06 Hz. The fluid is modelled as an added mass to the structure and Poisson coupling helps to model the interaction between fluid and structure. The graph shows that the proposed shell based CFM gives a good match with the results presented by Binulal et al.

The numerical program using shell elements is then validated using the experimental results available in the literature of Sharma et al. [18]. A copper U tube CFM is considered for the analysis. The properties of U tube CFM as well as conveying fluid and the excitation frequency of the CFM are given in Table 3. The maximum difference in the time lag found using present numerical formulation and the results given by S C Sharma is found to be 8.81%. Fig. 10(c) shows the comparison which reveals that the result obtained from the numerical code agrees with the experimental results shown by S C Sharma. The numerical program is also validated using the shell model proposed by Kutin et al. [21] for a straight circular cylindrical shell clamped at both ends conveying incompressible fluid. The properties of straight tube Coriolis mass flow meter used for the validation is given in table 4. The maximum difference in the time lag found out using the present shell formulation and the results presented by Kutin et al. is 0.32%. Fig. 10 (d) shows that the result from the numerical program agrees with the result presented by Kutin et al. for the shell Coriolis mass flow meter.

### *4.4. Experimental and numerical investigation of the changes in natural frequency of silicone tube*

Estimation of the excitation frequency of CFM is essential [50] even if the flow measuring tube is a metal tube. Generally, the tube is excited at its fundamental frequency to minimise the energy required for excitation. Hence the influence of pre-stretch on the fundamental frequency of the silicone tube is studied numerically and experimentally. Table 1 presents the parameters utilised for the numerical analysis of the natural frequency of the flexible tube. Table 5 displays the fundamental natural frequency of the silicone tube for an initial length of 25 cm. The tube is excited in X-Z plane, while responses along both the X-Z as well as X–Y plane are studied. Graphs display numerous undulations for the coherence function in the range of 20–25 Hz.

Fig. 11 (a) presents the Frequency response function, and the coherence function for the tube along the X-Z plane (horizontal plane). The first fundamental frequency (First bending mode) along X-Z plane (Horizontal plane) is observed as 21.6 Hz, while the tube experiences the same first bending mode of vibration along X–Y plane (Vertical plane) at a frequency of 25.8 Hz. Hence there is a difference in the first fundamental natural frequency of the tube measured along X-Z as well as X–Y plane. This difference in natural frequency exhibits the random vibrations due to the beat phenomenon occurred in a sagged tube, as reported by Krishna et al. [49]. The sagging of flexible tube results in the transition of the circularity in the cross-section to some uncertain shape like teardrop shape. The pre-stretching reduces sagging and thus, the difference in frequency observed in various planes of vibration also decreases. The difference in natural frequency seems to be 1.7 Hz for 10% pre-stretched tube while the difference in frequency reduces to 0.1 Hz for 20% pre-stretched tube. Table 5 shows the difference in first fundamental frequency found along X–Y plane and X-Z plane for 25 cm long tube containing water.

The numerical analysis of a cylindrical silicone tube of 25 cm initial length shows the same rising trend for the natural frequency while pre-stretching. The result is given in table 6. The Numerical static analysis is initially conducted with the pre-defined pre-stretched length to recognise the pre-stretch load required in the natural frequency analysis of the flexible tube. The geometric stiffness of the structure is found out based on the pre-stretched load and it gets added with the initial stiffness of the tube. The numerical analysis does not take care of the shape change due to sagging; instead, it treats the silicone tube as a merely cylindrical shell carrying fluid. Hence the change in natural frequency of the tube along various planes of vibration cannot be recognised in the numerical analysis.

**Table 6**
Numerical evaluation of First fundamental frequency of 25 cm (initial length) tube.

| Sl No | Length of tube (cm) | Pre-Stretch load for Geometric stiffness (N) | First Natural Frequency (Hz) |
|---|---|---|---|
| 1 | 25 + 1.25 cm Pre stretch | 6.5 | 24.16 |
| 2 | 25 + 2.5 cm Pre stretch | 15.3 | 25.12 |
| 3 | 25 + 3.75 cm Pre stretch | 18.5 | 26.14 |
| 4 | 25 + 5 cm Pre stretch | 24.6 | 26.82 |

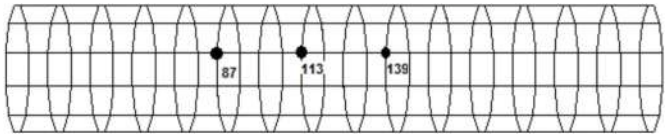


**Fig. 12.** Meshed model obtained from MATLAB.

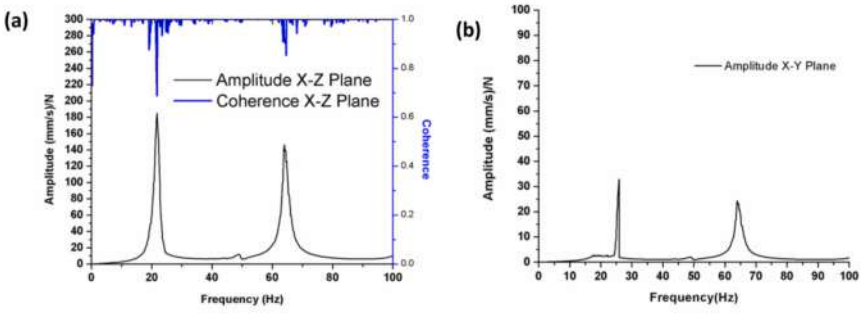


**Fig. 11.** FRF and Coherence plot for 5% Pre-stretched tube (a) FRF and Coherence along X-Z Plane (b) FRF along X–Y Plane.

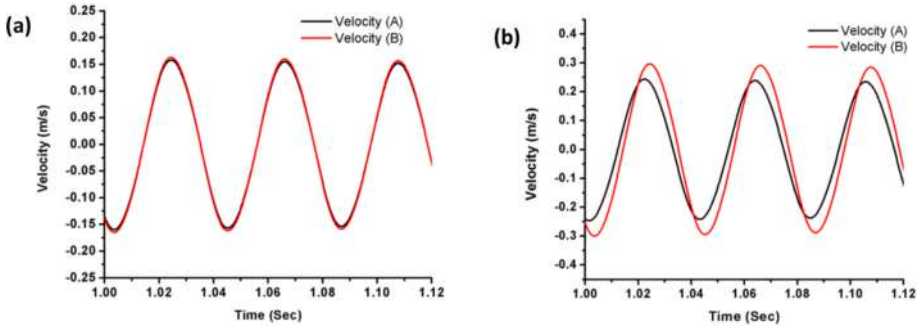


**Fig. 13.** (a) 10% pre-stretch – No flow (b) 10% -flow velocity 2.5 m/s (Excitation frequency – 25.1 Hz).

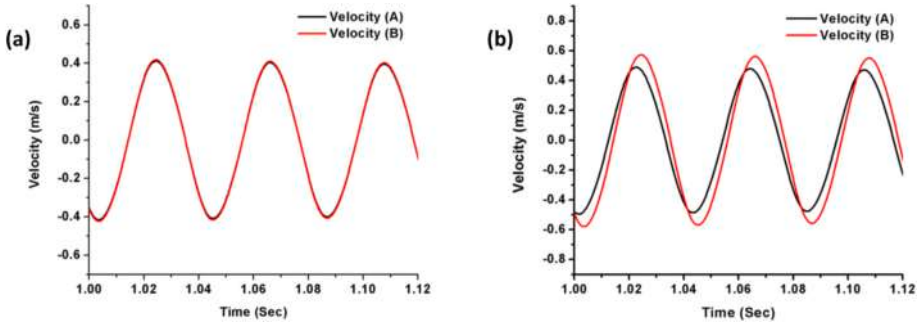


**Fig. 14.** (a) 15% Pre-stretch – No flow (b) 15% -flow velocity −2.5 m/s (Excitation frequency – 26.1 Hz).

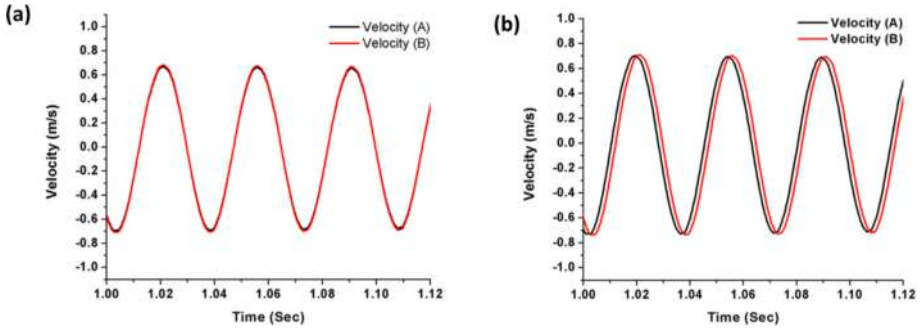


**Fig. 15.** (a) 20% Pre-stretch – No flow (b) 20% -flow velocity −2.5 m/s (Excitation frequency – 26.9 Hz).

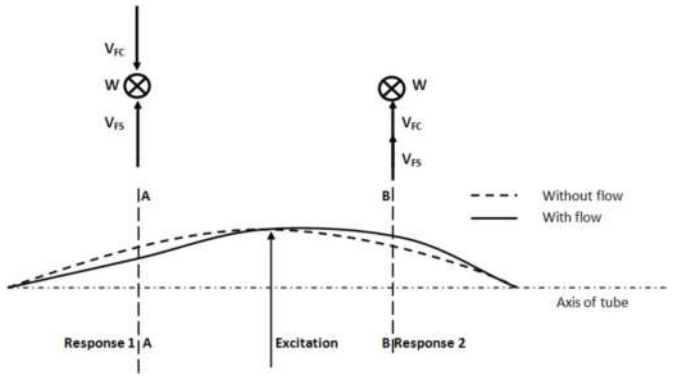


**Fig. 16.** Velocity of structure due to Coriolis forces and excitation. (W represents weight of fluid and shell, $V_{FC}$ – Velocity of Structure due to Coriolis forces, $V_{FS}$ – Velocity of Structure due to Excitation force).

For low pre-stretched tubes, the numerical natural frequency found to be different from the experimental natural frequency of flexible silicone tube. The numerical natural frequency corresponding to 20% pre-stretched flexible tube yields a value agreeing to the experimental natural frequency. This study shows that the pre-stretching promotes the tube to regain its cylindrical shape and reduces the change in natural frequency as well as the beat phenomenon.

### *4.5. Experimental investigation on the time lag of straight tube CFM*

The response of the CFM made up of flexible tubes is examined using a silicone tube of 25 cm initial length. The tube is excited at its centre, and the responses of two equidistant points from the excitation point are acquired. A MATLAB programme helps to identify the zero-crossing point of the response signals. Fig. 12 shows the meshed model used in the Matlab program to find the charecterestics of CFM. A sinusiodal excitation force is applied at node number 113, while the responces are picked from nodes 87 and 139. The no-flow condition observes no phase difference, while there is a phase shift when the fluid flows through the tube. Here the phase shift gives an idea of the mass flow rate, while the velocity response shows a difference in the amplitude of structure

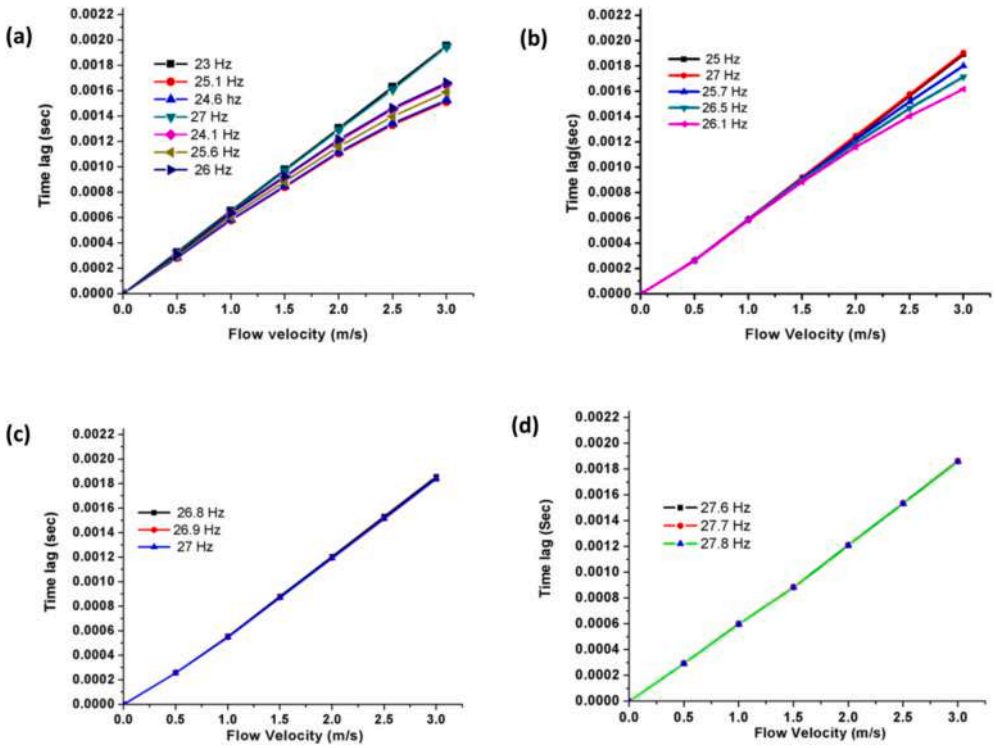


**Fig. 17.** Experimental Time lag for 25 cm long tube with (a) 10% pre-stretch (b) 15% pre-stretch(c) 20% (d) 25%.

velocity between the two points. The difference in structural velocity is found by Binulal et al. [24] and Stephanie Enz [51] but overlooked further analysis on the velocity change, as they concentrated on the phase shift alone. The change in structural velocity depends on the pre-stretching of the tube. The amplitude change of velocity reduces concerning the pre-stretching of the silicone tube.

Fig. 13 (a) shows the cross-correlation of the Coriolis flowmeter made up of a silicone tube of length 25 cm and a pre-stretch of 10% of its original length. The tube carrying fluid (no flow) shows no phase shift, while the tube conveying fluid with a flow velocity (2.5 m/s) shows a phase shift in the velocity responses picked from two points. Fig. 13(b) shows the response of the CFM with a flow velocity of 2.5 m/s. The responses show that the amplitude of velocities picked from the responses shows a difference. The Pre-stretching reduces the change in amplitude of structural velocity. The responses of CFM using the flexible tube with 15% and 20% pre-stretches are shown in Figs. 14 and 15 respectively. The change in amplitude of structural velocity happens typically due to the combined effect of Coriolis force and velocity of the structure due to excitation.

Fig. 16 shows the effect of excitation, Coriolis force and structural velocity on the flexible tube with and without fluid flow. As the tube is excited at its centre, the Coriolis force acting on one side of the tube along with the velocity of the tube produces an inward deflection of the tube (Section A-A). In contrast, the response of the second point (Section B–B), which includes the Coriolis force in the opposite direction and the tube velocity, results in an outward movement of the tube. This change in the direction of Coriolis force induces a difference in the response amplitude of structural velocity. For isotropic materials with a higher modulus of elasticity, the change in amplitude of structural velocity is not very significant compared to the change in amplitude of velocity observed in the silicone rubber tube. The flexible tube suffers from the effect of sagging, results in more twisting of the tube and hence the phase shift differs. Hence it can be inferred that the effect of change in amplitude of the structural velocity gets reflected in the phase shift between two points of the structure. The effect prevails more if the structure is flexible. The 20% pre-stretched tube shows a very little difference in the amplitude of structural velocities picked from the two equidistant points. The tube oscillations become smoother compared to the oscillations at lower pre-stretches.

The experimental research on the low pre-stretched tube reveals that there is a non-linearity in the calibration curve while the tube is operating at Coriolis frequency in the beat frequency region of the flexible

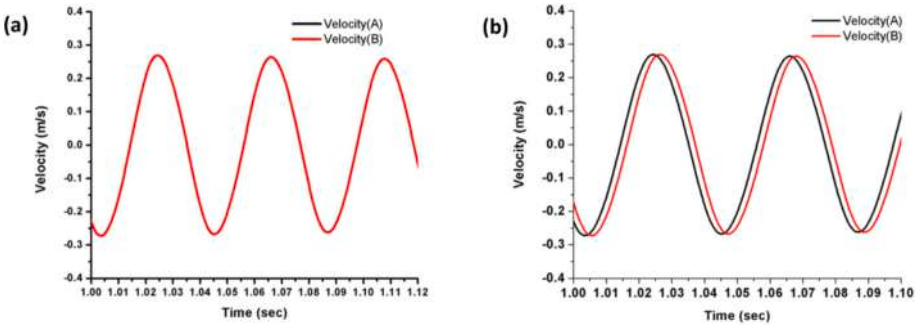


**Fig. 18.** Cross correlation for silicone tube 10% pre-stretch (a) No Flow (b) Flow velocity of 2.5 m/s.

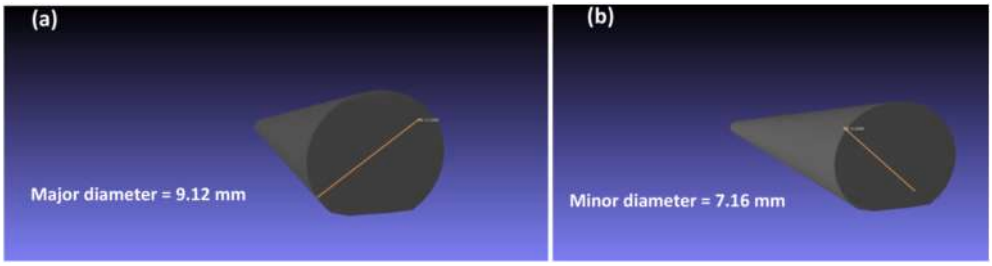


**Fig. 19.** Actual outer surface image of 5% Pre-stretched tube (a) Major Diameter (b) Minor Diameter.

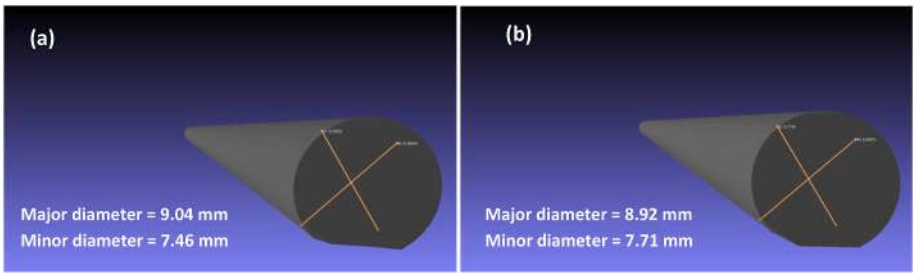


**Fig. 20.** Actual outer surface image of Silicone tube (a) 10% Pre-stretch (b) 15% Pre-stretch.

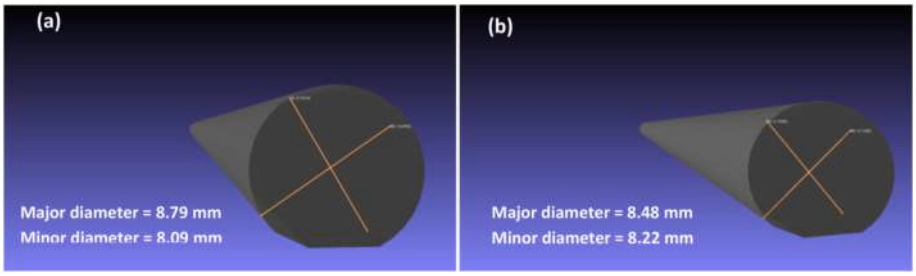


**Fig. 21.** Actual outer surface image of Silicone tube (a) 20% Pre-stretch (b) 25% Pre-stretch.

tube. Fig. 17 (a)–(d) describes the experimental time lag observed due to the phase shift in CFM made up of flexible silicone tubes. The 10% pre-stretched tube has got the first fundamental frequency along the horizontal as well as vertical plane as 24.3 Hz and 26 Hz respectively. Hence while the tube is excited at a frequency which is in between 24.3 Hz and 26 Hz, the tube follows a plane for vibration, which may not be the plane of excitation. Hence a nonlinear calibration curve can be observed for the CFM if it is excited in the beat frequency region. This non-linearity in the calibration curve reflects in the sensitivity of the Coriolis flowmeter. Hence, as the flow velocity increases, the sensitivity declines if the meter is operating in this beat frequency region. The result shows that as the excitation frequency increases the sensitivity first decreases, and later it develops. If the tube is excited at the frequency beyond the frequency range of 24.3 Hz and 26 Hz shows a linear trend for the calibration curve.

Similarly, the extent of non-linearity of the calibration curve for the CFM using flexible tubes reduces in the beat frequency range as the tube undergoes pre-stretching. This effect is because the difference in first

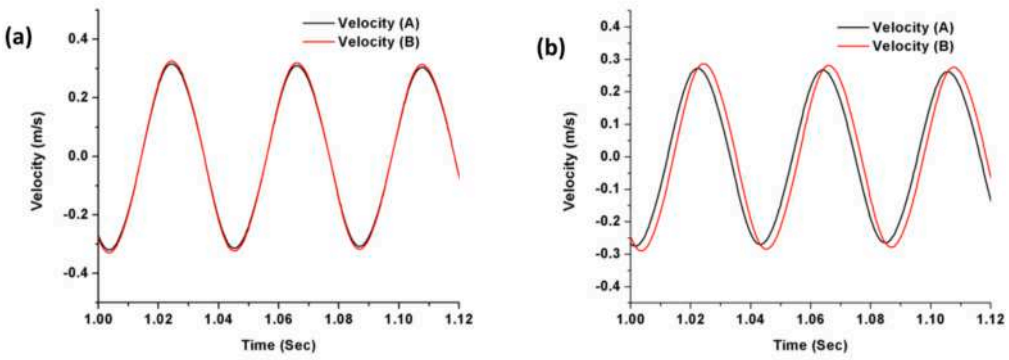


**Fig. 22.** Numerical analysis with actual shape of 10% pre-stretched silicone tube (a) No fluid flow (b) Flow velocity of 2.5 m/s.

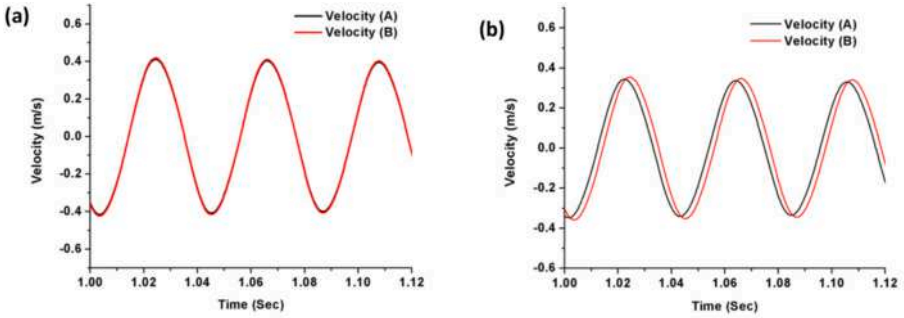


**Fig. 23.** Numerical analysis with actual shape of 20% pre-stretched silicone tube (a) No fluid flow (b) Flow velocity of 2.5 m/s.

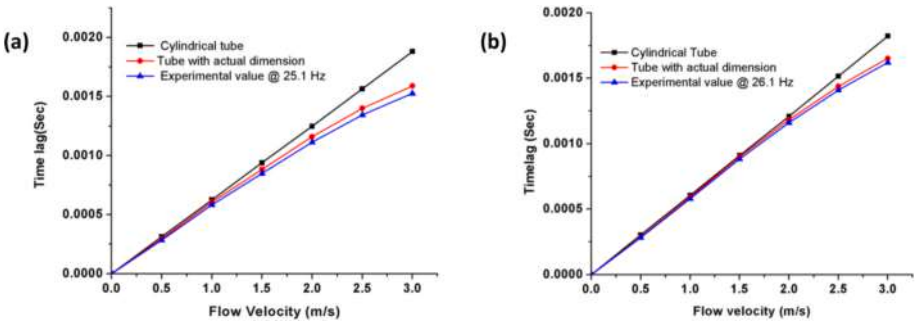


**Fig. 24.** Experimental and numerical analysis with actual shape and cylindrical shape (a) 10% (b) 15%.

fundamental frequency in two perpendicular planes reduces to 0.1 Hz as the tube is pre-stretched to 20% of its initial length. Hence the beat frequency of 0.1 Hz for a 20% pre-stretched tube means the tube behaves like a straight cylindrical structure; hence the tube offers a constant sensitive CFM made up of flexible tube.

### 4.6. Numerical analysis of 10% pre-stretched silicone tube

Fig. 18 (a) and (b) presents the numerical analysis of 10% pre-stretched tube with a circular cross-section. Fig. 18 (a) shows the responses from two points without any fluid flow, while 18 (b) shows the phase shift for a flow velocity of 2.5 m/s. There is no phase shift or amplitude of velocity variation for the stationery fluid-carrying tube, while the fluid conveying tube shows a phase shift. The amplitude of velocity from two points differs by a small value. Hence, these results show that the difference in amplitude of the velocity picked from two equidistant points predominates if the numerical analysis incorporates the effect of sagging.

### 4.7. Numerical analysis based on actual dimensions of silicone tube

The difference in sensitivity of the CFM made up of silicone tubes is due to the effect of sagging. The controlled excitation along either horizontal or vertical plane did not retain the tube vibrations in the plane of excitation. Hence the tube vibrates in a plane which may not be purely vertical or horizontal, rather would be some inclined plane. Also, the actual cross-section of the tube won't remain circular; rather, it seems to be in the shape of the teardrop, which leads to the tube oscillations in the apparent plane. The Laser scanning technique described by Krishna et al. [49] helps to identify the actual shape and dimensions of the tube. Figs. 19–21 represents the laser-scanned surfaces of tubes with 5%, 10%, 15%, 20% and 25% pre-stretch of the initial length. The major and minor diameter of the 5% pre-stretched tubes is identified as 9.12 mm and 7.16 mm respectively. Similarly the major and minor diameter

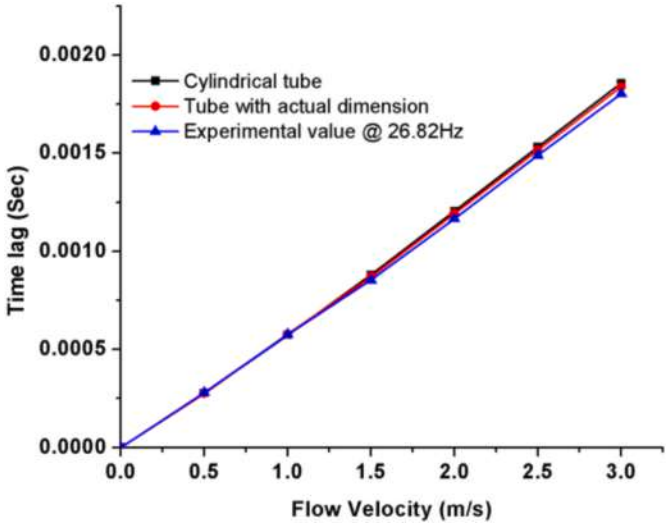


**Fig. 25.** Experimental and numerical analysis with actual shape and cylindrical shape with 20% pre-stretch.

of the 10% pre-stretched tubes is measured as 9.04 mm and 7.46 mm respectively. The major diameter reduces to 8.48 mm and the minor diameter increases to 8.22 mm for the 25% pre-stretched tube.

Fig. 22 (a) and (b) represents the numerical analysis of the CFM with 10% pre-stretched silicone tube. The results show that the sagging influences the amplitude of velocity picked from two equidistant points of excitation. The cross correlation for no flow condition indicates no phase shift, but shows a small change in amplitude of velocity. Hence the amplitude of velocity change will be an indication of the effect of sagging. The fluid flow causes a phase shift in the velocity response, while the amplitude of velocity also seems to be increasing with the increase of

flow velocity. Fig. 23 (a) and (b) represents the cross correlation for the CFM with 20% pre-stretched silicone tube. The no flow condition shows any phase difference and the amplitude variation is also negligible. The difference in amplitude of velocity reduces further compared to 10% pre-stretched tube.

The calibration curve obtained using the actual dimensions of the tube are agreeing exactly with the experimental data. Fig. 24 (a) shows the calibration curves for 10% pre-stretched tube. The tube analysed using cylindrical structure gains a linear calibration curve, while the calibration curves are non-linear for the tube with actual dimensions. This non-linear calibration curve follows the same trend of results obtained for experimental investigation. Hence it can be inferred that the sagging in flexible tube results in non-linearity in calibration curves.

Fig. 24 (b) represents the calibration curves obtained for the tube with 15% pre-stretch. The non-linearity observed for this 15% pre-stretched tube is reduced compared to the nonlinearity of 10% pre-stretched tube. The calibration curve obtained for a 20% pre-stretched tube shows almost a linear variation (Fig. 25). Hence it can be inferred that the pre-stretching increases the sensitivity of flexible tube CFM.

## 5. Conclusion

The paper describes the development of a numerical model for CFM using eight noded isoparametric shell elements and twenty noded three-dimensional acoustic fluid elements. A Matlab program is developed for solving the finite element equations for evaluating the characteristics of the Coriolis mass flow meter. The Matlab code for the numerical analysis of flexible tubes conveying fluid and assessing the characteristics of Coriolis mass flow meter is validated with the results available in the literature. The experimental calibration curve obtained for the CFM made up of flexible silicone tube is not linear; while the numerical calibration curve obtained using an initially straight cylindrical flexible tube is linear. This non-linearity in the calibration curve is due to the beat phenomenon encountered as a result of sagging. The laser scanning technique using FARO laser scanner aids to acquire the actual shape and dimensions of the sagged flexible tube. The numerical and experimental analysis on the Coriolis mass flow meter reveals that the amplitude of velocity measured from two equidistant points of the excitation shows some difference, and this difference lowers as the tube is pre-stretched.

The numerical and experimental analysis on the CFM made up of flexible tubes points that the change in amplitude of velocities measured along the equidistant points of excitation is significant in comparison to metal tubes for which it is negligible. Hence for flow measuring devices using flexible tubes, never ignore the influence of sagging of tubes as the beat phenomenon due to sagging can cause the tube to vibrate in an arbitrary plane other than the excitation plane. This beat phenomenon results in the variation of the amplitude of tube deflection, which indirectly alters the time lag due to phase shift. The numerical and experimental results show that the pre-stretching reduces the effect of sagging and promotes the tube to retrieve its circular cylindrical shape which in turn nullifies the change of frequency of vibration in horizontal and vertical directions perpendicular to the tube. Hence the pre-stretched flexible tubes can be used in flow measuring devices which use vibrational techniques. The shell model developed for the CFM is capable of predicting characteristics of the flexible structure, including sagging, stretch and beat accurately. For the flexible tube in the present case, a 20% stretch increases the extent of the linear region in the calibration curve. So, one can use a flexible tube with stretch in CFM, which in turn reduces the power required for the tube excitation and increases the range of operation as well as the sensitivity of the CFM.

## Credit author statement

R. Kamal Krishna, Methodology, Finite element Formulation, Experimental Investigation, Validation, Writing – original draft. M Unnikrishnan, Experimental Investigation, Resources finding, Validation, Writing – original draft, Supervision. Jayaraj Kochupillai, Conceptualization, Detailed Methodology, Finite element Formulation, Validation, Writing – original draft, Supervision

## Declaration of competing interest

We have no conflicts of interest to disclose.

## References

[1] B.R. Binulal, Akash Rajan, Jayaraj Kochupillai, Dynamic analysis of Coriolis flowmeter using Timoshenko beam element, Flow Meas. Instrum. 47 (2016) 100–109.
[2] P. Michael, Païdoussis, Fluid-Structure Interactions, Slender Structures and Axial Flow second ed., vol. 1, 2014. ISBN: 978-0-12-397312-2.
[3] P. Michael, Païdoussis, Fluid-Structure Interactions, Slender Structures and Axial Flow first ed., vol. 2, 2017. ISBN: 978-0-12-397333-7.
[4] Ming Ji, Kazuaki Inaba, Farid Triawan, Vibration characteristics of cylindrical shells filled with fluid based on first-order shell theory, J. Fluid Struct. 85 (2019) 275–291.
[5] Kochupillai Jayaraj, N. Ganesan, Padmanabhan Chandramouli, A semi-analytical coupled finite element formulation for shells conveying fluids, Comput. Struct. 80 (2002) 271–286.
[6] M. Amabili, K. Karagiozis, M.P. Paidoussis, Effect of geometric imperfections on non-linear stability of circular cylindrical shells conveying fluid, Int. J. Non Lin. Mech. 44 (2009) 276–289.
[7] Eleonora Tubaldi, Marco Amabili, Michael P. Païdoussis, 'Fluid–structure interaction for nonlinear response of shells conveying pulsatile flow', J. Sound Vib. 371 (2016) 252–276.
[8] Yong Liang Zhang, Daniel G. Gorman, Jason M. Reese, Vibration of pre-stressed thin cylindrical shells conveying fluid, Thin-Walled Struct. 41 (2003) 1103–1127.
[9] J Sadowski Adam, J. Michael Rotter, Solid or shell finite elements to model thick cylindrical tubes and shells under global bending, Int. J. Mech. Sci. 74 (2013) 143–153.
[10] Alireza Keramat, Kolahi Arash Ghaffarian, Ahmadi Ahmad, Waterhammer modelling of viscoelastic pipes with a time-dependent Poisson's ratio, J. Fluid Struct. 43 (2013) 164–178.
[11] J. Ruoff, M. Hodapp, H. Kück, Finite element modelling of Coriolis mass flowmeters with arbitrary pipe geometry and unsteady flow conditions, Flow Meas. Instrum. 37 (2014) 119–126.
[12] Samer Guirguis, Fan Shang Chun, Modeling of Coriolis mass flow meter of a general plane-shape pipe, Flow Meas. Instrum. 21 (2010) 40–47.
[13] L.J. Wang, L. Hua, Z.C. Zhu, P. Ye, X. Fu, Analytical calculation of sensitivity for Coriolis mass flowmeter, Measurement 44 (2011) 1117–1127.
[14] Jon Juel Thomsen, Jonas Dahl, Analytical predictions for vibration phase shifts along fluid-conveying pipes due to Coriolis forces and imperfections, J. Sound Vib. 329 (2010) 3065–3081.
[15] Ming Li, Manus Henry, Feibiao Zhou, Michael Tombs, Two-phase flow experiments with Coriolis Mass Flow Metering using complex signal processing, Flow Meas. Instrum. 69 (2019) 101613.
[16] Qi-Li Hou, Ke-Jun Xu, Min Fang, Cui Liu, Wen-Jun Xiong, Development of Coriolis mass flowmeter with digital drive and signal processing technology, ISA (Instrum. Soc. Am.) Trans. 52 (2013) 692–700.
[17] Felix Leach, Salah Karout, Feibiao Zhou, Michael Tombs, Martin Davy, Manus Henry, Fast Coriolis mass flow metering for monitoring diesel fuel injection, Flow Meas. Instrum. 58 (2017) 1–5.
[18] Satish C. Sharma, Pravin P. Patil, Major Ashish Vasudev, S.C. Jain, Performance evaluation of an indigenously designed copper (U) tube Coriolis mass flow sensors, Measurement 43 (2010) 1165–1172.
[19] L. van de Ridder, W.B.J. Hakvoort, J. van Dijk, J.C. Lötters, A. de Boer, Quantification of the influence of external vibrations on the measurement error of a Coriolis mass-flowmeter, Flow Meas. Instrum. 40 (2014) 39–49.
[20] N. Mole, G. Bobovnik, J. Kutin, B. Stok, I. Bajsic, 'An improved three-dimensional coupled fluid–structure model for Coriolis flowmeters', J. Fluid Struct. 24 (2008) 559–575.
[21] J. Kutin, I. Bajsic, Characteristics of the shell-type Coriolis flowmeter, J. Sound Vib. 228 (2) (1999) 227–242.
[22] G. Bobovnik, N. Mole, J. Kutin, B. Stok, I. Bajsic, Coupled finite-volume/finite-element modelling of the straight-tube Coriolis flowmeter, J. Fluid Struct. 20 (2005) 785–800.
[23] Rosa Monge, Jarno Groenesteijn, Dennis Alveringh, R.J. Wiegerink, Joost Lötters, Luis J. Fernandez, 'SU–8 micro Coriolis mass flow sensor', Sensor. Actuator. B 241 (2017) 744–749.
[24] B.R. Binulal, Akash Rajan, M. Unnikrishnan, Jayaraj Kochupillai, Experimental determination of time lag due to phase shift on a flexible pipe conveying fluid, Measurement 83 (2016) 86–95.
[25] C. Clark, M. Zamora, R. Cheesewright, M. Henry, The dynamic performance of a new ultra-fast response Coriolis flow meter, Flow Meas. Instrum. 17 (2006) 391–398.
[26] C. Clark, R. Cheesewright, The influence upon Coriolis mass flow meters of external vibrations at selected frequencies, Flow Meas. Instrum. 14 (2003) 33–42.

[27] C. Clark, S. Wang, R. Cheesewright, The performance characteristics of a micro-machined Coriolis flow meter: an evaluation by simulation, Flow Meas. Instrum. 17 (2006) 325–333.
[28] A. Svete, J. Kutin, G. Bobovnik, I. Bajsić, Theoretical and experimental investigations of flow pulsation effects in Coriolis mass flowmeters, J. Sound Vib. 352 (2015) 30–45.
[29] R. Cheesewright, Simon Shaw, Uncertainties associated with finite element modelling of Coriolis mass flow meters, Flow Meas. Instrum. 17 (2006) 335–347.
[30] Richard Smith, Sparks Douglas, Diane Riley, Nader Najafi, A MEMS-based Coriolis mass flow sensor for industrial applications, IEEE Trans. Ind. Electron. 56 (4) (April 2009).
[31] Peter Enoksson, Goran Stemme and Erik Stemme, 'A Coriolis mass flow sensor structure in silicon', Proceedings of Ninth International Workshop on Micro Electromechanical Systems, 11-15 Feb. 1996, ISBN: 0-7803-2985-6.
[32] R. Kamal Krishna, Jayaraj Kochupillai, 'A new formulation for fluid–structure interaction in pipes conveying fluids using Mindlin shell element and 3-D acoustic fluid element', J. Braz. Soc. Mech. Sci. Eng. 42 (2020) 388.
[33] M. Amabili, Non-linear vibrations of doubly curved shallow shells, Int. J. Non Lin. Mech. 40 (2005) 683–710.
[34] Klaus-Jurgen Bathe, Finite Element Procedures, Prentice Hall, 1996. ISBN 0-13-301458-4.
[35] Ebrahim Asadi, S. Mohamad, Qatu, 'Static analysis of thick laminated shells with different boundary conditions using GDQ', Thin-Walled Struct. 51 (2012) 76–81.
[36] Ana Amaro Maria Augusta Neto, Luis Roseiro, José Cirne, Rogério Leal, Engineering Computation of Structures: the Finite Element Method, Springer International Publishing Switzerland, 2015. ISBN 978-3-319-17709-0.
[37] F. Alijani, M. Amabili, K. Karagiozis, F. Bakhtiari-Nejad, Nonlinear vibrations of functionally graded doubly curved shallow shells, J. Sound Vib. 330 (2011) 1432–1454.
[38] Ansel c. Ugural, Plates and Shells Theory and Analysis, CRC Press Taylor & Francis Group, 2018.
[39] G.R. Liu, S.S. Quek, The Finite Element Method: A Practical Course, Butterworth-Heinemann, 2003. ISBN 0 7506 5866 5.
[40] Dávid Visy, Sándor Ádány, Local elastic and geometric stiffness matrices for the shell element applied in cFEM, Period. Polytech. Civ. Eng. 61 (3) (2017) 569–580.
[41] Maurice Petyt, Introduction to Finite Element Vibration Analysis, ISBN 978-0-521-19160-9, second ed., Cambridge University Press.
[42] Eugenio Onate, Structural Analysis with the Finite Element Method Linear Statics Vol 2, Beams, Plates and Shells, first ed., International Center for Numerical Methods in Engineering (CIMNE), 2013. ISBN: 978-1-4020-8742-4.
[43] Eleonora Tubaldi, Marco Amabili, Michael P. Païdoussis, 'Fluid–structure interaction for nonlinear response of shells conveying pulsatile flow', J. Sound Vib. 371 (2016) 252–276.
[44] Ashok K Jain, Dynamics of Structures with Matlab Applications, first ed., Pearson India Education Services Pvt Ltd, 2016. ISBN 978-93-325-5855-7.
[45] Joze Kutin, Andrej Smrecnik, Ivan Bajsic, 'Phase-locking control of the Coriolis meter's resonance frequency based on virtual instrumentation', Sensor. Actuator. 104 (2003) 86–93.
[46] Madhusudanan Unnikrishnan, Akash Rajan, Binulal Basanthvihar Raghunathan, Jayaraj Kochupillai, Dynamic testing of a pre-stretched flexible tube for identifying the factors affecting modal parameter estimation, J. Inst. Eng. India Ser. C 98 (2017) 421–430.
[47] Vibration Testing: Theory and Practice, Kenneth G McConnell, John Wiley, and Sons.
[48] M.P. Païdoussis, Flutter of conservative systems of Pipes conveying incompressible fluid, J. Mech. Eng. Sci. 17 (1975).
[49] R. Kamal Krishna, M.R. Mahesh, Madhusudanan Unnikrishnan, Jayaraj Kochupillai, Effect of sagging on dynamic characteristics of silicone tube conveying fluid, J. Inst. Eng. India Ser. C 101 (2) (2020) 241–256.
[50] R. Cheesewright, C. Clark, A. Belhadj, Y.Y. Hou, The dynamic response of Coriolis mass flow meters, J. Fluid Struct. 18 (2003) 165–178.
[51] Stephanie Enz, Thomsen Jon Juel, Predicting phase shift effects for vibrating fluid-conveying pipes due to Coriolis forces and fluid pulsation, J. Sound Vib. (2011) 5096–5113. Vol 330.